mater.scichina.com link.springer.com

Published online 15 July 2022 | https://doi.org/10.1007/s40843-022-2099-9
Sci China Mater 2022, 65(11): 2958–2966

MXene-mediated regulation of local electric field surrounding polyoxometalate nanoparticles for improved lithium storage

Huixia Chao[1], Yanan Li[1], Yukun Lu[1], Yazhen Yao[1], Yifan Zhu[1], Hao Yang[1], Kai Wang[2], Yi Wan[1], Qian Xu[1], Lu Guan[1], Han Hu[1*] and Mingbo Wu[1*]

ABSTRACT **Due to their capability of reversibly accepting multi lithium ions, polyoxometalates (POMs) have been widely regarded as promising candidates for electrochemical lithium storage. Nevertheless, the insulating nature of POMs hinders fast migration kinetics of lithium within the bulk of these materials. Herein, we propose the introduction of a local electric field surrounding the POM nanoparticles consisting of Mn and V where the concomitant Coulomb forces can accelerate the migration of lithium ions. After rationally hybridizing POMs with MXene nanosheets, the imbalanced charge distribution emerging at their interface produces the local electric field, thereby leading to a 250-fold increase of lithium diffusion coefficient. In this regard, a capacitive contribution as high as 81.7% at 1.0 mV s^{-1} is observed. Moreover, the POM nanoparticles could densely assemble on the surface of MXene nanosheets, offering highly packed electrodes and thus high volumetric capacities. Due to the improved lithium-ion transfer kinetics, the POMs/MXenes composites are paired with activated carbon to produce lithium-ion capacitors which could offer a high energy density of 195.5 W h kg^{-1} and a large power capability of 3800 W kg^{-1}. The findings in this work could build a clear relationship between materials with different conductivities for designing electrode materials.**

Keywords: local electric field, polyoxometalate nanoparticles, MXenes, lithium storage

INTRODUCTION

The serious resource and environmental issues caused by the overconsumption of fossil fuels accelerate the construction of an electrified society [1]. In this regard, lithium-ion batteries (LIBs) and other lithium-based energy storage devices [2,3], for example, lithium-ion capacitors (LICs), have been extensively explored for energy storage and utilization [4,5]. These devices are mainly based on the lithium intercalation chemistry on graphite anodes [6,7]. However, such a mechanism could only permit a low specific capacity and sluggish kinetics, prohibiting the graphite-based anode to fulfill the increasing demand on energy storage devices [8]. To address this issue, tremendous efforts have been devoted to searching for anode materials with alternative mechanisms [9]. Among all the potential candidates, polyoxometalates (POMs) represent one of the most promising candidates [10–14]. As a typical kind of molecular cluster, POMs are generally made of more than three transition metal oxyanions. Of particular note is that POMs could reversibly accept multi lithium ions and electrons, affording a large specific capacity for lithium storage [15]. In addition, the transition metals within POMs could be regulated in a wide range, producing various redox chemistry [16,17]. Because of these merits, a myriad of POMs have been explored for reversible lithium storage.

Despite their promising prospect for robust lithium storage, POMs encounter a series of challenges for practical application. One key aspect is their intrinsically insulating nature which requires a relatively large number of conductive additives to facilitate the charge transfer within the POM-based electrodes [18,19]. As a result, the nanostructured POMs have been widely assembled with various conductive substrates. Awaga's group [20] decorated $(n\text{-}Bu_4N)_3[PMo_{12}O_{40}]$ POMs on the surface of carbon nanotubes (CNTs) and realized a 23% increase in the specific capacity. Song's team [21] employed CNTs to thread the POM nanocrystals where the composites afforded a specific capacity of 850 mA h g^{-1} for over 100 cycles. In addition to CNTs, graphene represents another widely used conductive substrate to load POMs. Liu *et al.* [22] dispersed $Na_2H_8[MnV_{13}O_{38}]$ POMs (VM POMs) on the surface of reduced graphene oxide (rGO) and observed one order of magnitude increased ion diffusion coefficient. Nevertheless, the fundamental mechanisms underlying the performance improvement caused by these hybrid structures have seldom been elaborately investigated. This results in insufficient utilization of POMs for lithium storage. Recently, the local electric field generated between components of different conductivities has been proposed to effectively regulate the lithium storage performance [23,24]. The key rule is the *in-situ* generated local electric field leading to a Coulomb force for accelerating lithium diffusion. As a result, the rich local electric field could promote the practical performance of the electrodes.

Herein, the POM nanoplates consisting of V and M are loaded on Ti_3C_2X nanosheets for lithium storage. The hybridization of two types of two-dimensional (2D) nanostructures could produce rich interfaces. Because of the excellent conductivity of MXenes, a larger local electric field is afforded compared with other conductive substrates, for example rGO, being employed. As a result, the as-obtained composites offer a decent lithium

[1] State Key Laboratory of Heavy Oil Processing, Institute of New Energy, College of Chemical Engineering, China University of Petroleum (East China), Qingdao 266580, China
[2] College of Electrical Engineering, Qingdao University, Qingdao 266071, China
[*] Corresponding authors (emails: hhu@upc.edu.cn (Hu H); wumb@upc.edu.cn (Wu M))

storage performance with a large specific capacity of 600 and 370 mA h g^{-1} at the current density of 100 and 1000 mA g^{-1}, respectively, and an excellent pseudocapacitive contribution of 81.7% at a scan rate of 1.0 mV s^{-1}, superior to the POM alone and POMs/rGO composites. Moreover, the composites could be directly packed into a highly compacted structure when harvesting, allowing a volumetric capacity as high as 410 mA h cm^{-3} at a current density of 1000 mA g^{-1} after 2000 cycles. After pairing with activated carbon (AC) to produce the LICs, a promising electrochemical performance is obtained. The finding in this work may inspire a new route to design novel electrode materials for energy storage applications.

EXPERIMENTAL SECTION

Materials preparation

VM POMs were synthesized according to a previously reported method with minor modification [22]. First, 0.52 mol of $NaVO_3$ was dissolved in 1000 mL of water along with adding 40 mL of HNO_3 (1.0 mol L^{-1}) solution and 40 mL of $MnSO_4$ (1.0 mol L^{-1}) solution. Then, 80 mmol of $Na_2S_2O_8$ was introduced. After that, the mixed solution was heated to 70°C to gradually evaporate extra water till the volume of the mixed solution was reduced to 600 mL. The precipitate was removed and the remained solution was aged for 3–4 days to precipitate out the orange crystals, which are the VM POMs. To prepare the Ti_3C_2X nanosheets [25,26], 2.0 g of Ti_3AlC_2 powder (11 technology Co., LTD, China) was dispersed in 40 mL of HCl (9 mol L^{-1}) solution and then 2.0 g of LiF was introduced to trigger the etching process for 28 h at 35°C. Then, the supernate was removed after centrifuging at 3500 r min^{-1} for 10 min. After re-dispersion of the sediment in deionized water, another centrifugation and supernate removal were conducted. The dispersion, centrifugation, and supernate removal processes were repeated until the pH of the supernate reached 6.0. Finally, the precipitate was re-dispersed in water to produce the aqueous dispersion of MXenes for subsequent use.

rGO was prepared *via* the following steps. (1) Pre-oxidization of graphite: 6.0 g of graphite, 4.2 g of $K_2S_2O_8$, and 6.2 g of P_2O_5 were added to 300 mL of concentrated H_2SO_4. After heating at 80°C for 5.0 h under continuous stirring, the mixed solution was cooled down to room temperature naturally, and 2000 mL of deionized H_2O was added to the above dispersion. The pre-oxidized graphite was obtained through vacuum filtration and subsequent drying. (2) Preparation of graphene oxide (GO): 2.5 g of the pre-oxidized graphite was added to 300 mL of concentrated H_2SO_4 in an ice bath, 10 g of $KMnO_4$ was slowly added to the solution and then the solution was stirred at 35°C for 4 h. Then, 2000 mL of deionized H_2O and 15 mL of H_2O_2 (35%) were slowly added to the mixed dispersion. The obtained slurry was then centrifuged and washed repeatedly with dilute HCl (V_{H_2O}:V_{HCl} = 10:1), and then GO was obtained by washing with deionized water until the pH reached 7. (3) Reduction of GO: 0.15 g of GO and 75 mL of ethylene glycol ($C_2H_6O_2$) were mixed and sonicated for 1.0 h, and then, heated at 160°C for 17 h in a hydrothermal vessel. The as-collected precipitate was washed repeatedly with acetone, ethanol, and water, and then dried at 65°C for 12 h to produce rGO.

To prepare the VM POMs/MXenes, 50.0 mL of VM POM dispersion (10 mg mL^{-1}) was prepared, and then mixed with 100 mL of MXene dispersion (5 mg mL^{-1}). After stirring for 48 h, the product was collected by freeze-drying. The mass ratio of VM POMs to MXenes in the composite was set as 1:1. The VM POMs/rGO was prepared using the identical procedure except replacing the MXenes with rGO.

Materials characterization

To acquire the crystal structures of different samples, X-ray diffraction (XRD) patterns were recorded on an X' Pert PRO MPD diffractometer equipped with Cu Kα radiation (λ = l.5406 Å). A series of imaging instruments, including JEOL SM-7900F scanning electron microscopy (SEM), JEM-2010 transmission electron microscopy (TEM), FEI Talos 200S scanning TEM (STEM), and MultiMode SPM atomic force microscopy (AFM) were used to observe the morphology of the as-obtained materials and elemental mapping were conducted on a DI MULTIMODE system. A HORIBA HR800 spectrometer was employed to detect the Raman spectra of the materials using an excitation laser of 512 nm. To analyze the chemical bonding, X-ray photoelectron spectroscopy (XPS) was measured on an Escalab 250XI system with Al Kα radiation (Thermo Fisher Scientific). The thermal gravimetric analysis (TGA) curves were obtained on a thermal gravimetric analyzer (PerkinElmer TGA 4000) with a heating rate of 10°C min^{-1} in nitrogen. The element contents were collected using Agilent 710 inductively coupled plasma-atomic emission spectrometry (ICP-AES). The electrical conductivity was tested using the two-probe method.

Electrochemical measurements

To carry out the electrochemical measurements, the working electrodes were firstly prepared using the following procedure. The active material, carbon black, and sodium carboxymethyl cellulose (CMC) at a mass ratio of 8:1:1 were grinded with the assistance of deionized water to produce a slurry. The as-prepared slurry was then coated on the metal-foil current collectors and vacuum dried at 100°C for 12 h, after which the electrodes were produced. A typical CR2032 coin-cell was assembled by pairing the working electrode with Li foil as the counter and reference electrodes with 1 mol L^{-1} $LiPF_6$ in dimethyl carbonate (DMC), ethylene carbonate (EC), and ethyl methyl carbonate (EMC) (1:1:1 vol%) and 2.0 wt% fluoroethylene carbonate (FEC) as the electrolyte. The galvanostatic charge and discharge (GCD) profiles and cyclic stabilities were recorded using a NEWARE BTS-5V Measurement System while cyclic voltammetry (CV) curves and electrochemical impedance spectroscopy (EIS) were obtained on an IVIUMn STAT electrochemical workstation. The Li^+ diffusivities of the VM POMs/MXenes electrode were measured by galvanostatic intermittent titration technique (GITT) with a pulse current of 200 mA g^{-1} and a 15 min rest interval.

Density functional theory (DFT) calculation

For a reliable calculation, the Perdew-Burke-Ernzerhof (PBE) functional under the generalized gradient approximation (GGA) was set as the base [27,28]. The projector augmented wave (PAW) method was used in the Vienna *ab initio* simulation package (VASP) [29]. The Monkhorst-Pack scheme of *k*-points mesh was set to 3 × 3 × 1. The plane-wave cutoff energy was set to be 450 eV. The convergence threshold for the self-consistent field was set to 10^{-4} eV for the electronic relaxation and 0.02 eV $Å^{-1}$ for the maximum forces of each atom. The DFT-D3 method was used to consider the van der Waals interactions. Here, the 2D transition metal carbide, Ti_3C_2, was constructed by

sandwiched Ti and C atom layers, which consists of three Ti layers and two C layers, forming edge-shared octahedral structures. rGO was modelled by loading oxygen-containing functional groups on graphene nanosheets. According to the experiment results, we can see that VM POM has a layered structure and is mainly composed of multiple duplicate molecular clusters of $Na_2H_8[MnV_{13}O_{38}]$. Therefore, to simulate VM POMs, $Na_2H_8[MnV_{13}O_{38}]$ was first obtained according to the previous results of powder XRD data and the optimized structure with lattice parameters a = 10.80 Å and c = 20.73 Å was well fit with the powder diffraction pattern.

According to the experimental characterization, MXenes and VM POMs can form heterostructures by overlapping each other. In order to simplify the calculation, we cut along the c direction and got a layer structure of $Na_2H_8[MnV_{13}O_{38}]$, and a molecular cluster was finally selected to interact with Ti_3C_2 in a single cell. A molecular cluster of $Na_2H_8[MnV_{13}O_{38}]$ consisted of 13 distorted edge-shared VO_6 octahedra surrounding a central MnO_6 octahedron. To investigate the interaction between Ti_3C_2 and $Na_2H_8[MnV_{13}O_{38}]$, the charge density difference was analyzed by the equation:

$$\Delta\rho = \rho_{total} - \rho_{Ti_3C_2} - \rho_{POMs}, \quad (1)$$

where ρ_{total}, $\rho_{Ti_3C_2}$ and ρ_{POMs} are the charge densities for total adsorbed systems, Ti_3C_2 and $Na_2H_8[MnV_{13}O_{38}]$. The charge density difference of the POMs/rGO composite was obtained by replacing the charge density of MXene with that of rGO in Equation (1).

RESULTS AND DISCUSSION

Fig. 1a illustrates the fabrication process of the VM POMs/MXenes composites. To obtain rich interfaces, POMs with a 2D structure, specifically, nanoplate, are selected. The POMs used in this work mainly consist of V and Mn, and were prepared according to a previous report [30]. The detailed structure of VM POMs is revealed in Figs S1 and S2. Powder XRD shows that VM POM particles possess good crystallinity (Fig. S1a), whose cellular structure chart was inserted in Fig. S1a. TGA reveals that the VM POMs contain 12 crystalline H_2O molecules per molecule which could be completely removed by heating up to 250°C, accounting for a weight loss of ~12.9 wt%, as illustrated in Fig. S1b. ICP-AES analysis reveals the molar ratio of Mn:V:Na is 1:12.8:2.2 in VM POMs, indicating a composition of 1 Mn, 13 V, and 2 Na atoms. High-resolution XPS (HRXPS) of V 2p demonstrates that the ratio of V^{IV}:V^{V} in VM POMs is close to 3:10 (Fig. S1c) [22,31]. As a result, the formula of VM POMs can be determined as $Na_2H_8[MnV_{13}O_{38}]\cdot 12H_2O$. The VM POMs feature nanoplate morphology under SEM observation in Fig. S2a, which was further confirmed by TEM characterization (Fig. S2b). The HRTEM image of the nanoplate shows a lattice fringe spacing of 0.25 nm (Fig. S2c), corresponding to the (002) plane of VM POMs. MXene nanosheets used here are the most

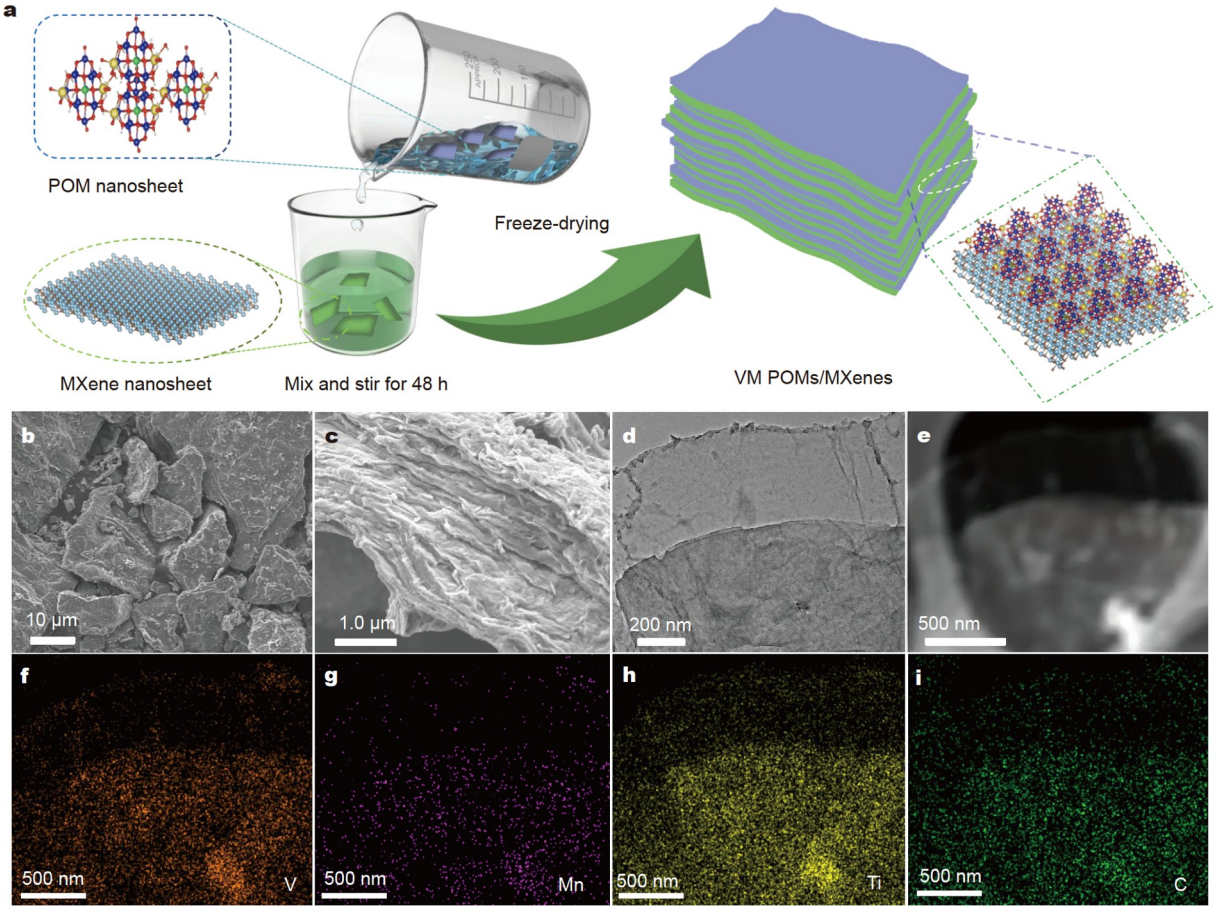

Figure 1 (a) The schematic illustration of fabricating the VM POMs/MXenes composites. (b, c) SEM images of VM POMs/MXenes at different magnifications. (d) TEM image of VM POMs/MXenes. The HAADF TEM image of the composite (e) and the related elemental mappings of V (f), Mn (g), Ti (h), and C (i).

typical one, namely, the Ti_3C_2X nanosheets which were obtained through etching the Ti_3AlC_2 MAX phase in an aqueous solution of HCl containing LiF [32,33], as reflected in Figs S3 and S4. The as-prepared MXene nanosheets are highly dispersible in water as shown in Fig. S3a and the XRD patterns reveal that Ti_3AlC_2 MAX was completely etched to generate Ti_3C_2X MXenes (Fig. S3b). Then, the two aqueous dispersions of VM POM nanoplates and MXene nanosheets were mixed and stirred for 48 h. The VM POMs/MXene composites were obtained after a subsequent freeze-drying process. The whole materials synthesis was carried out at ambient conditions without complex equipment, thus holding promising prospects for the mass production. An interesting finding in this work is the highly stacked structure of the as-obtained product. Specifically, the VM POM nanoplates firmly adhere to the surface of MXene, which are then stacked heavily into a compact structure, as revealed by SEM (Fig. 1b). Such a structure may allow the as-prepared materials a large density that secures a high volumetric performance. Specifically, the tap density and coating density could be as high as 1.3 and 1.49 g cm^{-3}, respectively. From the side view of the heavily stacked particles (Fig. 1c), the flat sheet structure is largely tortuous compared with the original MXene nanosheets, suggesting the stacking of the components with different sizes. Fig. 1d reflects the TEM image of VM POMs/MXene composites. The transparent sheet under the electron beam indicates the ultrathin thickness and the VM POMs are uniformly decorated on the surface of MXenes. In contrast to the bare MXene nanosheets (Fig. S4a), the composite is less smooth. Moreover, the element distribution under high-angle annular dark-field (HAADF) imaging, as shown in Fig. 1e–i, reveals the highly uniform distribution of V (Fig. 1f), Mn (Fig. 1g), Ti (Fig. 1h), and C (Fig. 1i), originated from the two components.

Then, the structural details of the composite were further characterized by XRD and XPS spectra. The XRD pattern of the composite (Fig. 2a) reveals the combined band of VM POMs and MXenes, but with an essentially reduced intensity. This may suggest that the stacking manner of VM POMs in the composite is much different from that of the pure POMs. As revealed from the VM POMs, the POMs are heavily stacked into a thick nanoplate (Fig. S2). In the presence of MXene nanosheets, the subunit of VM POMs uniformly adheres to the surface of MXenes, giving an essentially decreased intensity. The XPS full-spectra of the VM POMs/MXenes, MXenes, and VM POMs are compared in Fig. 2b. Obviously, the signal from all the related elements could be detected in the spectra. The comparison of the detailed spectra of Mn (Fig. 2c) and V (Fig. 2d) reveals the shift of binding energy [34,35], indicating the formation of chemical bonds between the VM POMs and MXenes.

To evaluate the lithium storage performance, half-cells were fabricated with VM POMs/MXenes as the working electrode and the lithium foils as the reference and counter electrodes. Meanwhile, the electrochemical performance of VM POMs and MXenes was also measured. The GCD profiles of VM POMs/MXenes are shown in Fig. 3a. By increasing the current density from 0.1 to 4.0 A g^{-1}, no obvious plateaus are observed in these curves, indicating the excellent rate capability. The specific capacity is 627, 512, 433, 371, 309, and 244 mA h g^{-1} at current densities of 0.1, 0.2, 0.5, 1.0, 2.0, and 4.0 A g^{-1}, corresponding to volumetric specific capacity of 934, 763, 645, 553, 460, and 363 mA h cm^{-3}, respectively, superior to other results reported elsewhere (Table S1) [36–45]. Then, the rate performance of the VM POMs/MXenes is shown in Fig. 3b. The specific capacity is

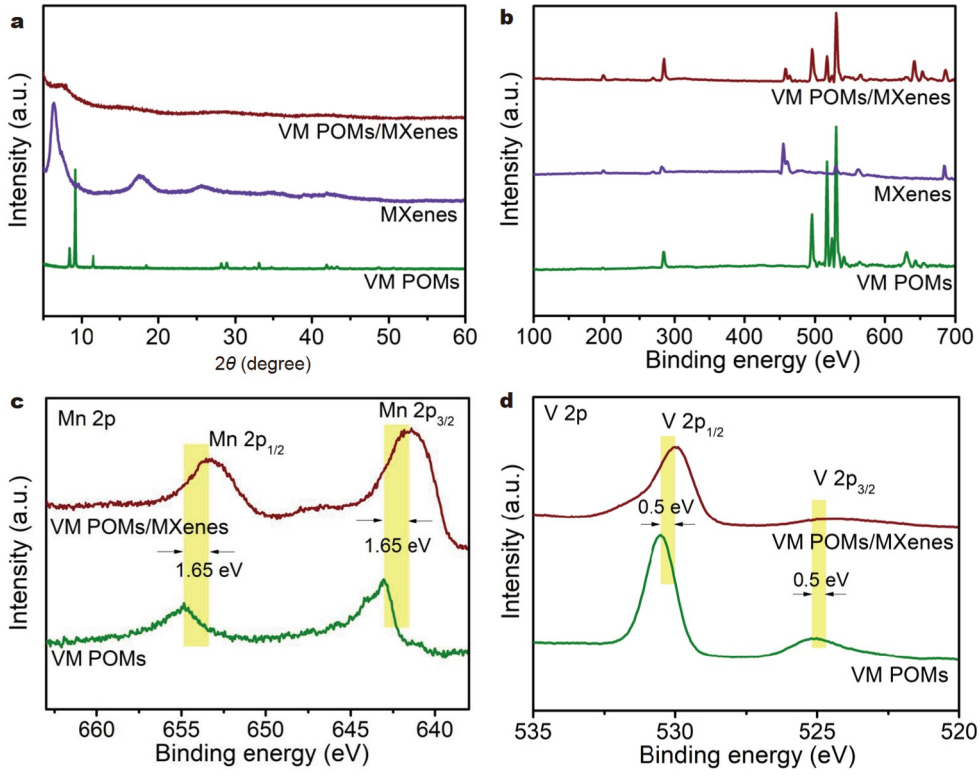

Figure 2 (a) XRD patterns and (b) XPS spectra of VM POMs, MXenes, and VM POMs/MXenes. HR XPS profiles of (c) Mn 2p and (d) V 2p of VM POMs/MXenes and VM POMs.

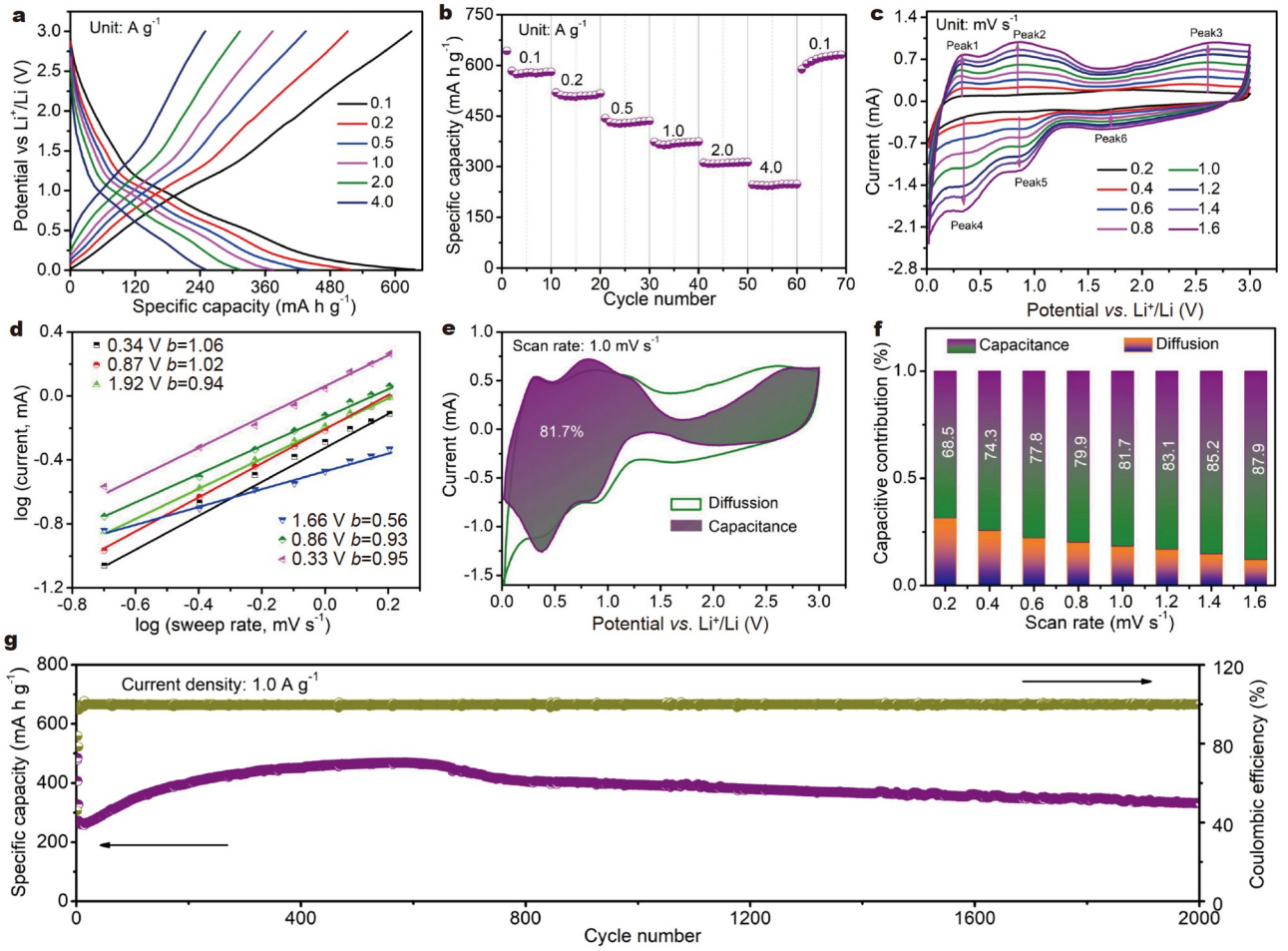

Figure 3 Lithium storage performance of VM POMs/MXenes. (a) GCD curves at various current densities. (b) Rate capability measured at the current densities from 0.1 to 4.0 A g^{-1}. (c) CV tests at varying scan rates from 0.2 to 1.6 mV s^{-1}. (d) *b*-value analysis. (e) Evaluation of the capacitive current at a scan rate of 1.0 mV s^{-1} and (f) capacitive contributions at different scan rates. (g) Cycling performance recorded at 1.0 A g^{-1} for 2000 cycles.

gradually decreased with the increase of the current densities. Nevertheless, the corresponding specific capacity of the composite is larger than that of the single components (Figs S5 and S6). To unravel the lithium storage kinetics, the relationship of current density (i) and the scan rate (v) was determined using the following equation [46,47]:

$$i = av^b. \quad (2)$$

In this equation, both parameters of a and b are adjustable and the value of b is widely used to determine the lithium storage kinetics. Firstly, the CV curves of VM POMs/MXenes at different current densities were recorded in Fig. 3c and the peak currents at different potentials were collected to calculate the b value. The b value of 0.5 indicates a diffusion-controlled process, while 1.0 means a surface-dominated manner. As shown in Fig. 3d, the b values larger than 0.9 are delivered at potentials ranging from 0.3 to 2.7 V *vs.* Li/Li^+, suggesting surface-dominated processes in a wide potential range. Then, the contribution of the aforementioned two processes to the current is separated using the following equation [48,49]:

$$i(V) = k_1v + k_2v^{1/2}, \quad (3)$$

where k_1v, k_2v, and $i(V)$ represent a capacitive effect-induced current, diffusion-controlled Li^+ insertion process, and the total current response, respectively, at a given potential V. Fig. 3e exhibits the CV curve of the VM POMs/MXenes at a scan rate of 1.0 mV s^{-1} which offers a capacitive contribution of 81.7%. Even at a scan rate as low as 0.2 mV s^{-1}, the capacitive contribution can still be as high as 68.5% (Fig. 3f). These results suggest that the VM POMs/MXenes mainly adopt a pseudocapacitive effect for charge storage, which is a highly demanded behavior for power-type energy storage devices [50], for example LICs. In contrast, the kinetics behavior of VM POMs exhibited in Fig. S7 is inferior to that of the composite [51]. To reveal the improved performance experimentally, the Nyquist plots of the composite and VM POMs were compared. As shown in Fig. S8, the composite shows a much smaller transfer resistance and a smaller circle at the high-frequency range. Then, the diffusion coefficients of Li^+ (D_{Li^+}) of the two materials during charge and discharge were acquired using the GITT [52]. The calculated values are plotted as a function of the potential during charge and discharge, as shown in Figs S9 and S10. The D_{Li^+} values of VM POMs/MXenes remain between 1.0×10^{-10}–6.0×10^{-10} cm^2 s^{-1} in the potential range of 0.0 and 2.7 V *vs.* Li/Li^+ (Fig. S9a–c), which is about 250-fold higher than that of VM POMs (Fig. S10a–c). Moreover, the cycling performance of the composite is also superior to that of the VM POMs. As shown in Fig. 3g, the composite offers a capacity retention of almost 100% after 2000 cycles, superior to VM POMs (Fig. S5d), MXenes (Fig. S6c) and other related structures (Table S2) [53–56].

The local electrical field at the interface plays a crucial role in the boosted electrochemical performance where the larger difference in electrical conductivity between different components, the better [24,57,58]. To verify this viewpoint, another POM-based composite with a lower conductive 2D substrate, rGO, was prepared using a similar procedure for electrochemical analysis. The electrical conductivity of MXene nanosheets (1460 S m^{-1}) is two order of magnitude higher than that of rGO nanosheets (16 S m^{-1}). As shown in Figs S11 and S12, the VM POMs/rGO shows an inferior performance to the VM POMs/MXenes. To get an insight into the role of the local electric field, DFT calculations were carried out. The charge density distribution shown in Fig. 4a, b indicates that a more pronounced electron transfer occurs at the interface of MXenes and VM POMs (6.6 e) which may be associated with a larger difference in electric conductivity. As a result, the positive and negative centers would be built at different components. The larger charge density difference was further confirmed in the curve of the planar-averaged electron density difference ($\Delta\rho$) in Fig. 4c. Obviously, the electron density difference at the MXenes and VM POMs interface of VM POMs/MXenes is larger than that of their rGO-based counterpart. The essentially improved charge transfer behavior facilitated by the highly conductive MXene nanosheets is conducive to the local electric field effect, thereby significantly accelerating the charge transfer [23,59].

In view of the enhanced rate capability and cycle stability, we used VM POMs/MXenes as the anode and commercial AC as the cathode to construct a full LIC, and the structural analysis and electrochemical performances of the AC were provided in our previous research [60]. To balance the charge between the two electrodes, the optimized mass ratio of cathode/anode was determined to be about 1.2. The pairing processes of anode and cathode are shown in Fig. 5a, where the CV curve of the full device is also offered. Obviously, a decent capacitive capability is provided as reflected from the quasi-rectangle CV curves of the full device. The highly symmetrical GCD curves were obtained

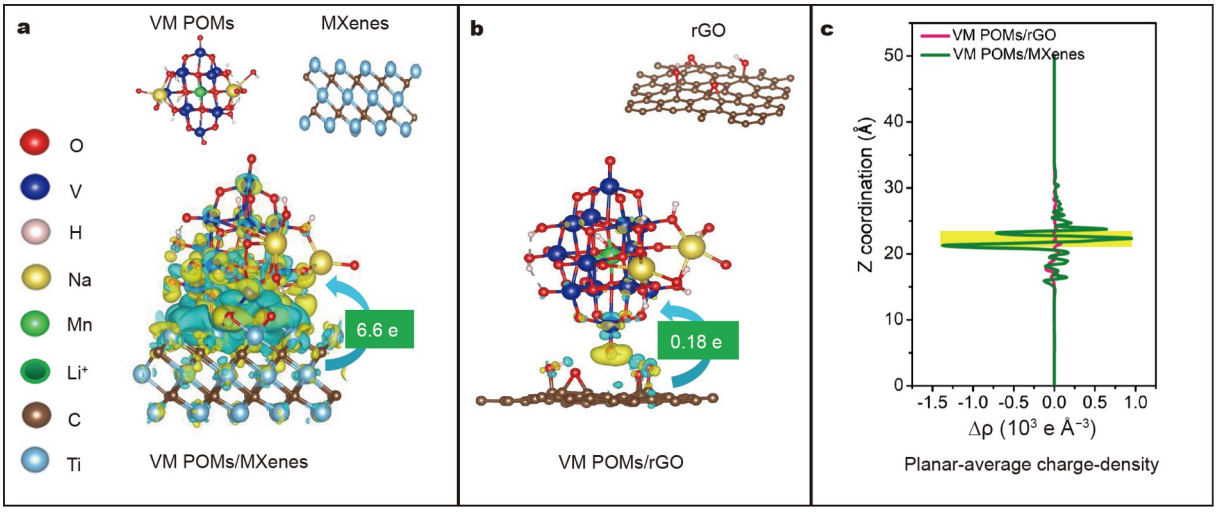

Figure 4 Theoretical calculations of the charge density distribution in (a) VM POMs/MXenes and (b) VM POMs/rGO. (c) The planar-averaged charge density difference $\Delta\rho$ for VM POMs/MXenes and VM POMs/rGO.

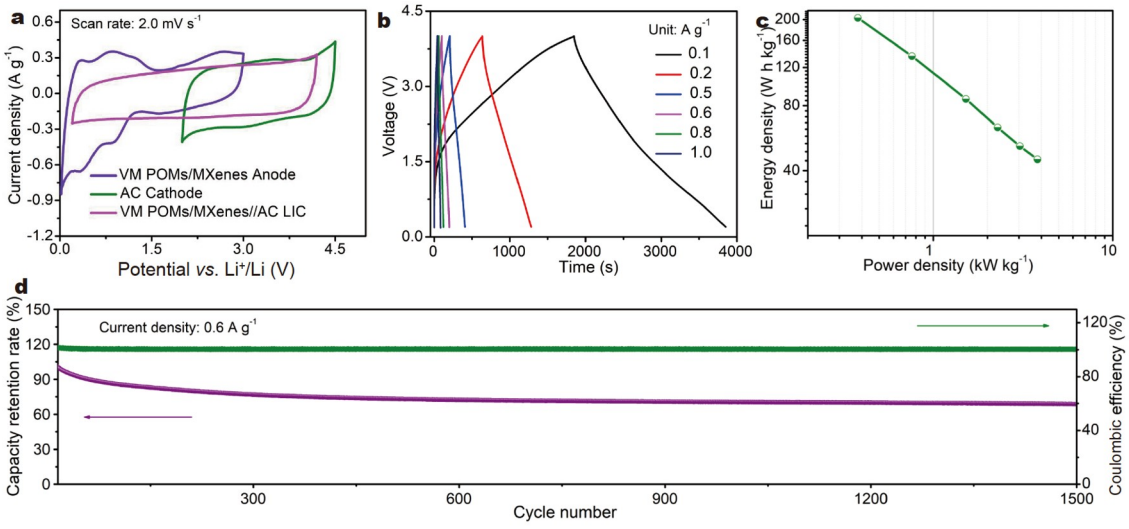

Figure 5 Electrochemical performance of the LIC with VM POMs/MXenes as the anode. (a) CV curves of the anode, cathode, and the LIC at a scan rate of 2.0 mV s^{-1}. (b) GCD curves of the LICs at current densities ranging from 0.1 to 1.0 A g^{-1}. (c) Ragone plot, and (d) cycling performance of the LIC.

at a series of current densities ranging from 0.1 to 1.0 A g^{-1} as shown in Fig. 5b. Meanwhile, the potential range of the anode and cathode was simultaneously recorded using the three-electrode split cell (Fig. S13) [56,61]. As shown in Fig. S14a, the operating potential range of the anode and cathode is 0.2–2.4 and 2.6–4.0 V *vs.* Li^+/Li, respectively. The well-matched relationship could be maintained at different current densities because the potential profiles of both electrodes remain almost undistorted as illustrated in Fig. S14b [62]. This observation provides further evidence of the excellent pseudocapacitive behavior of VM POMs/MXenes for lithium storage [63,64]. In the full device, the charge transfer resistance is also quite low, as shown in Fig. S14c. The Ragone plot of the LIC is drawn to illustrate its practical performance. As exhibited in Fig. 5c, a high energy density of 195.5 W h kg^{-1} is obtained at a power density of around 380 W kg^{-1}, while a decent energy density of 45.0 W h kg^{-1} is still delivered even at a large power output of 3800 W kg^{-1}. Furthermore, the LIC exhibits a decent cycling performance with a capacity retention of 80.0% after 1200 cycles at a current density of 0.6 A g^{-1} (Fig. 5d), and the Coulombic efficiency is nearly 100% during the cycling test.

CONCLUSIONS

In summary, the concept of local electric field has been firstly applied to the POM-based anode material for lithium storage. The 2D VM POM nanoplates were hybridized with MXene nanosheets by simply mixing the dispersion of the two components and aging for a while, creating rich interfaces. Due to the significant difference of conductivity between composite components, an obvious charge transfer occurs at the interfaces, contributing to positive and negative centers locally. The local electric field is then built, facilitating the charge transfer. As a result, a substantially increased rate capability is produced with a capacitive contribution as high as 81.7% at a scan rate of 1.0 mV s^{-1}. In view of the high rate performance, a rate-capable device, LIC, was built by using the VM POMs/MXenes as the anode. The electrochemical characterization reveals the well-matched electrodes at various current densities. The as-fabricated LIC possesses excellent performance in terms of high energy density (195.5 W h kg^{-1}) and large power density (3800 W kg^{-1}). The investigation carried out in this work may shed light on the role of enhanced charge transfer induced by the local electric field and provides alternative ideas for designing composite materials for energy storage applications.

Received 6 March 2022; accepted 28 April 2022; published online 15 July 2022

1 Xu T, Li Z, Wang D, *et al.* A fast proton-induced pseudocapacitive supercapacitor with high energy and power density. Adv Funct Mater, 2022, 32: 2107720
2 Fang S, Shen L, Hoefling A, *et al.* A mismatch electrical conductivity skeleton enables dendrite-free and high stability lithium metal anode. Nano Energy, 2021, 89: 106421
3 Zhou J, Kang Q, Xu S, *et al.* Ultrahigh rate capability of 1D/2D polyaniline/titanium carbide (MXene) nanohybrid for advanced asymmetric supercapacitors. Nano Res, 2022, 15: 285–295
4 Zhou J, Xu S, Kang Q, *et al.* Iron oxide encapsulated in nitrogen-rich carbon enabling high-performance lithium-ion capacitor. Sci China Mater, 2020, 63: 2289–2302
5 Jagadale A, Zhou X, Xiong R, *et al.* Lithium ion capacitors (LICs): Development of the materials. Energy Storage Mater, 2019, 19: 314–329
6 Kong D, Qiu X, Wang B, *et al.* WS_2 nanoplates embedded in graphitic carbon nanotubes with excellent electrochemical performance for lithium and sodium storage. Sci China Mater, 2018, 61: 671–678
7 Natarajan S, Aravindan V. An urgent call to spent LIB recycling: Whys and wherefores for graphite recovery. Adv Energy Mater, 2020, 10: 2002238
8 Zhang H, Lv X, Wang F, *et al.* Vertically aligned, polypyrrole encapsulated MoS_2/graphene composites for high-rate LIBs anode. Ceramics Int, 2018, 44: 7611–7617
9 Han D, Zhang J, Weng Z, *et al.* Two-dimensional materials for lithium/sodium-ion capacitors. Mater Today Energy, 2019, 11: 30–45
10 Chen JJ, Symes MD, Fan SC, *et al.* High-performance polyoxometalate-based cathode materials for rechargeable lithium-ion batteries. Adv Mater, 2015, 27: 4649–4654
11 Wu HY, Hu H, Qin C, *et al.* Self-assembly and lithium storage performance of a nanoscale polyoxometalate based on the $\{MnTa_{18}\}$ cluster. Chem Commun, 2020, 56: 2403–2406
12 Meng X, Wang HN, Zou YH, *et al.* Polyoxometalate-based metallogels as anode materials for lithium ion batteries. Dalton Trans, 2019, 48: 10422–10426
13 Huang P, Wang XL, He DQ, *et al.* Two nanoscale Nb containing polyoxometalates based on $\{P_2W_{15}Nb_3O_{62}\}$ clusters and chromium cations. Dalton Trans, 2017, 46: 13345–13348
14 Wu HY, Huang M, Qin C, *et al.* Self-assembly and Li-ion storage performance of three new Nb/W mixed-addendum polyoxometalates based on the $\{SiNb_3W_9O_{40}\}$ clusters and transition-metal cations. CrystEngComm, 2019, 21: 1862–1866
15 Yang MH, Choi BG, Jung SC, *et al.* Polyoxometalate-coupled graphene *via* polymeric ionic liquid linker for supercapacitors. Adv Funct Mater, 2014, 24: 7301–7309
16 Hartung S, Bucher N, Chen HY, *et al.* Vanadium-based polyoxometalate as new material for sodium-ion battery anodes. J Power Sources, 2015, 288: 270–277
17 Zhao X, Niu G, Yang H, *et al.* MIL-88A@polyoxometalate microrods as an advanced anode for high-performance lithium ion batteries. CrystEngComm, 2020, 22: 3588–3597
18 Ye JC, Chen JJ, Yuan RM, *et al.* Strategies to explore and develop reversible redox reactions of Li-S in electrode architectures using silver-polyoxometalate clusters. J Am Chem Soc, 2018, 140: 3134–3138
19 Meng J, Lei M, Lai C, *et al.* Lithium ion repulsion-enrichment synergism induced by core-shell ionic complexes to enable high-loading lithium metal batteries. Angew Chem, 2021, 133: 23444–23454
20 Nishimoto Y, Yokogawa D, Yoshikawa H, *et al.* Super-reduced polyoxometalates: Excellent molecular cluster battery components and semipermeable molecular capacitors. J Am Chem Soc, 2014, 136: 9042–9052
21 Hu J, Ji Y, Chen W, *et al.* "Wiring" redox-active polyoxometalates to carbon nanotubes using a sonication-driven periodic functionalization strategy. Energy Environ Sci, 2016, 9: 1095–1101
22 Liu J, Chen Z, Chen S, *et al.* "Electron/ion sponge"-like V-based polyoxometalate: Toward high-performance cathode for rechargeable sodium ion batteries. ACS Nano, 2017, 11: 6911–6920
23 Liu Y, Zhou T, Zheng Y, *et al.* Local electric field facilitates high-performance Li-ion batteries. ACS Nano, 2017, 11: 8519–8526
24 Meng T, Li B, Wang Q, *et al.* Large-scale electric-field confined silicon with optimized charge-transfer kinetics and structural stability for high-rate lithium-ion batteries. ACS Nano, 2020, 14: 7066–7076
25 Abdolhosseinzadeh S, Jiang X, Zhang H, *et al.* Perspectives on solution processing of two-dimensional MXenes. Mater Today, 2021, 48: 214–240
26 Zhang CJ, Ma Y, Zhang X, *et al.* Two-dimensional transition metal carbides and nitrides (MXenes): Synthesis, properties, and electrochemical energy storage applications. Energy Environ Mater, 2020, 3: 29–55
27 Kresse G, Furthmüller J. Efficient iterative schemes for *ab initio* total-energy calculations using a plane-wave basis set. Phys Rev B, 1996, 54: 11169–11186
28 Kresse G, Hafner J. *Ab initio* molecular dynamics for open-shell transition metals. Phys Rev B, 1993, 48: 13115–13118
29 Blöchl PE. Projector augmented-wave method. Phys Rev B, 1994, 50:

17953–17979
30 Nagai K, Ichida H, Sasaki Y. The structure of heptapotassium tridecavanadomanganate(IV) octadecahydrate, $K_7[MnV_{13}O_{38}]\cdot 18H_2O$. Chem Lett, 1986, 15: 1267–1270
31 Zhang T, Pan L, Tang H, *et al.* Synthesis of two-dimensional $Ti_3C_2T_x$ MXene using HCl+LiF etchant: Enhanced exfoliation and delamination. J Alloys Compd, 2017, 695: 818–826
32 Lu X, Yu M, Zhai T, *et al.* Correction to high energy density asymmetric quasi-solid-state supercapacitor based on porous vanadium nitride nanowire anode. Nano Lett, 2020, 20: 6932
33 Flynn CM, Pope MT. 1:13 Heteropolyvanadates of manganese(IV) and nickel(IV). J Am Chem Soc, 2002, 92: 85–90
34 Ghidiu M, Lukatskaya MR, Zhao MQ, *et al.* Conductive two-dimensional titanium carbide 'clay' with high volumetric capacitance. Nature, 2014, 516: 78–81
35 Chen L, Ruan Y, Zhang G, *et al.* Ultrastable and high-performance Zn/VO_2 battery based on a reversible single-phase reaction. Chem Mater, 2019, 31: 699–706
36 Li L, Dong G, Xu Y, *et al.* H_3IDC-assisted synthesis of mesoporous ultrafine Co_3O_4/N-doped carbon nanowires as a high rate and long-life anode for lithium-ion batteries. J Alloys Compd, 2020, 818: 152826
37 Niu H, Yang Q, Wang Q, *et al.* Oxygen vacancies-enriched sub-7 nm cross-linked $Bi_{2.88}Fe_5O_{12-x}$ nanoparticles anchored MXene for electrochemical energy storage with high volumetric performances. Nano Energy, 2020, 78: 105360
38 Seo JH, Verlinde K, Rajagopalan R, *et al.* Cold sintering process for fabrication of a high volumetric capacity $Li_4Ti_5O_{12}$ anode. Mater Sci Eng-B, 2019, 250: 114435
39 Ge X, Gu C, Yao Z, *et al.* Pseudocapacitive material with 928 mA h cm^{-3} particle-level volumetric specific capacity enabled by continuous phase-transition. Chem Eng J, 2018, 338: 211–217
40 Zou F, Xu T, Wu Z, *et al.* Lithium and sodium adsorption on monolayer tellurene. J Phys Chem C, 2020, 124: 28074–28082
41 Chang B, Liu J, Qing G, *et al.* A high-tap-density nanosphere-assembled microcluster to simultaneously enable high gravimetric, areal and volumetric capacities: A case study of TiO_2 anode. J Mater Chem A, 2018, 6: 11916–11928
42 Haridas AK, Gangaja B, Srikrishnarka P, *et al.* Spray pyrolysis-deposited nanoengineered TiO_2 thick films for ultra-high areal and volumetric capacity lithium ion battery applications. J Power Sources, 2017, 345: 50–58
43 Liu YT, Wang L, Liu S, *et al.* Constructing high gravimetric and volumetric capacity sulfur cathode with $LiCoO_2$ nanofibers as carbon-free sulfur host for lithium-sulfur battery. Sci China Mater, 2021, 64: 1343–1354
44 Wang S, Zhang H, Zhang D, *et al.* Vertically oriented growth of MoO_3 nanosheets on graphene for superior lithium storage. J Mater Chem A, 2018, 6: 672–679
45 Yan X, Li T, Xiong Y, *et al.* Synchronized ion and electron transfer in a blue T-Nb_2O_{5-x} with solid-solution-like process for fast and high volumetric charge storage. Energy Storage Mater, 2021, 36: 213–221
46 Hao Y, Wang S, Shao Y, *et al.* High-energy density Li-ion capacitor with layered SnS_2/reduced graphene oxide anode and BCN nanosheet cathode. Adv Energy Mater, 2020, 10: 1902836
47 Zhou G, Wang DW, Yin LC, *et al.* Oxygen bridges between NiO nanosheets and graphene for improvement of lithium storage. ACS Nano, 2012, 6: 3214–3223
48 Niu S, Wang Z, Yu M, *et al.* MXene-based electrode with enhanced pseudocapacitance and volumetric capacity for power-type and ultralong life lithium storage. ACS Nano, 2018, 12: 3928–3937
49 Hu X, Liu Y, Chen J, *et al.* Fast redox kinetics in Bi-heteroatom doped 3D porous carbon nanosheets for high-performance hybrid potassium-ion battery capacitors. Adv Energy Mater, 2019, 9: 1901533
50 Jiang S, Yun S, Cao H, *et al.* Porous carbon matrix-encapsulated MnO *in situ* derived from metal-organic frameworks as advanced anode materials for Li-ion capacitors. Sci China Mater, 2022, 65: 59–68
51 Lai C, Dou YY, Li X, *et al.* Improvement of the high rate capability of hierarchical structured $Li_4Ti_5O_{12}$ induced by the pseudocapacitive effect. J Power Sources, 2010, 195: 3676–3679
52 Lu F, Xu C, Meng F, *et al.* Two-step synthesis of hierarchical dual few-layered Fe_3O_4/MoS_2 nanosheets and their synergistic effects on lithium-storage performance. Adv Mater Interfaces, 2017, 4: 1700639
53 Chen W, Huang L, Hu J, *et al.* Connecting carbon nanotubes to polyoxometalate clusters for engineering high-performance anode materials. Phys Chem Chem Phys, 2014, 16: 19668–19673
54 Ding YH, Peng J, Khan SU, *et al.* A new polyoxometalate (POM)-based composite: Fabrication through POM-assisted polymerization of dopamine and properties as anode materials for high-performance lithium-ion batteries. Chem Eur J, 2017, 23: 10338–10343
55 Hu J, Diao H, Luo W, *et al.* Dawson-type polyoxomolybdate anions ($P_2Mo_{18}O_{62}^{6-}$) captured by ionic liquid on graphene oxide as high-capacity anode material for lithium-ion batteries. Chem Eur J, 2017, 23: 8729–8735
56 Chao H, Qin H, Zhang M, *et al.* Boosting the pseudocapacitive and high mass-loaded lithium/sodium storage through bonding polyoxometalate nanoparticles on MXene nanosheets. Adv Funct Mater, 2021, 31: 2007636
57 Li B, Wang J, Cao Z, *et al.* The role of SnO_2 surface coating in the electrochemical performance of $Li_{1.2}Mn_{0.54}Co_{0.13}Ni_{0.13}O_2$ cathode materials. J Power Sources, 2016, 325: 84–90
58 Yan C, Zhu Y, Li Y, *et al.* Local built-in electric field enabled in carbon-doped Co_3O_4 nanocrystals for superior lithium-ion storage. Adv Funct Mater, 2018, 28: 1705951
59 Luo W, Li F, Li Q, *et al.* Heterostructured Bi_2S_3-Bi_2O_3 nanosheets with a built-in electric field for improved sodium storage. ACS Appl Mater Interfaces, 2018, 10: 7201–7207
60 Li K, Lu X, Zhang Y, *et al.* Bi_3TaO_7/Ti_3C_2 heterojunctions for enhanced photocatalytic removal of water-borne contaminants. Environ Res, 2020, 185: 109409
61 Qin H, Chao H, Zhang M, *et al.* Precious potential regulation of carbon cathode enabling high-performance lithium-ion capacitors. Carbon, 2021, 180: 110–117
62 Gómez-Urbano JL, Moreno-Fernández G, Arnaiz M, *et al.* Graphene-coffee waste derived carbon composites as electrodes for optimized lithium ion capacitors. Carbon, 2020, 162: 273–282
63 Dong J, He Y, Jiang Y, *et al.* Intercalation pseudocapacitance of $FeVO_4\cdot nH_2O$ nanowires anode for high-energy and high-power sodium-ion capacitor. Nano Energy, 2020, 73: 104838
64 Gogotsi Y, Penner RM. Energy storage in nanomaterials-capacitive, pseudocapacitive, or battery-like? ACS Nano, 2018, 12: 2081–2083

Acknowledgements This work was supported by the National Natural Science Foundation of China (21975258, 22179145, and 22138013), the Natural Science Foundation of Shandong Province (ZR2020ZD08), the startup support grant from China University of Petroleum (East China), and Taishan Scholar Project (ts201712020). The authors thank the valuable suggestion from Prof. Jilei Liu at Hunan University.

Author contributions Hu H and Wu M conceived the project. Chao H prepared the samples and conducted the tests; Li Y and Zhu Y carried out the DFT calculation; Lu Y, Yao Y and Yang H helped with the sample preparation and testing. Wang K, Wan Y, Xu Q, and Guan L helped with the sample characterizations. Chao H wrote the paper with support from Hu H. All authors contributed to the general discussion.

Conflict of interest The authors declare that they have no conflict of interest.

Supplementary information Supporting data are available in the online version of the paper.

Huixia Chao received her bachelor degree in 2004 from the University of Petroleum, and master degree in 2007 from Sinopec Research Institute of Petroleum Processing. Now, she is a PhD candidate at China University of Petroleum (East China). Her research interest mainly focuses on constructing novel electrode materials for advanced energy storage devices.

Han Hu is a professor at China University of Petroleum (East China). After receiving his PhD degree from Dalian University of Technology in 2014, he conducted postdoctoral research at Nanyang Technological University, Leibniz Institute, and The University of Queensland for 4 years before joining China University of Petroleum (East China) in 2018. His research interest concentrates on the design and controlled preparation of new energy materials and advanced carbon materials.

Mingbo Wu is a professor at the Institute of New Energy, China University of Petroleum (East China). He obtained his PhD degree from Dalian University of Technology in 2004. He has been awarded Taishan Scholar in 2017 and 10,000 Talent in 2018. His research interest includes the preparation of new carbon materials for applications in energy storage, catalysis, environmental protection and other fields.

MXene辅助调控杂多酸纳米颗粒局部电场增强其锂存储性能

晁会霞[1], 李雅楠[1], 卢玉坤[1], 姚亚珍[1], 朱一凡[1], 杨浩[1], 王凯[2], 万弋[1], 徐倩[1], 关露[1], 胡涵[1*], 吴明铂[1*]

摘要 杂多酸(POMs)具有可逆接收/脱除多个锂离子的能力, 被认为是具有广泛应用前景的电化学储锂材料. 然而, POMs的绝缘特性阻碍了锂离子在其中的快速迁移. 鉴于此, 我们提出在由Mn和V组成的POMs纳米颗粒周围引入局部电场, 通过同步产生的库仑力加速锂离子的迁移. 将POMs与MXenes纳米片复合后, 界面处的不平衡电荷分布诱导产生了局部电场, 使得锂扩散系数提高了250倍. 在1.0 mV s^{-1}的低扫速下, 复合材料赝电容贡献高达81.7%. 此外, POMs的纳米颗粒可以在MXene纳米片表面致密组装, 赋予电极材料高体积容量. 由于改善的锂离子传输动力学, POMs/MXenes复合材料与商业活性炭组装的锂离子电容器可输出195.5 W h kg^{-1}的能量密度和3800 W kg^{-1}的功率密度. 本研究为高性能电极材料的设计提供了新思路.

